Effects of amorphous silica on mechanical contribution of coarse aggregates in UHPC

DOI:
10.1016/j.cemconcomp.2023.105225

Document status and date:
Published: 01/09/2023

Document Version:
Publisher's PDF, also known as Version of Record (includes final page, issue and volume numbers)

Please check the document version of this publication:

• A submitted manuscript is the version of the article upon submission and before peer-review. There can be important differences between the submitted version and the official published version of record. People interested in the research are advised to contact the author for the final version of the publication, or visit the DOI to the publisher's website.
• The final author version and the galley proof are versions of the publication after peer review.
• The final published version features the final layout of the paper including the volume, issue and page numbers.

Link to publication

Effects of amorphous silica on mechanical contribution of coarse aggregates in UHPC: From micromechanics to mesoscale fracture and macroscopic strength

Shaohua Li [a], Yuxuan Chen [a,**], H.J.H. Brouwers [b], Qingliang Yu [a,b,*]

[a] School of Civil Engineering, Wuhan University, 430072, Wuhan, PR China
[b] Department of the Built Environment, Eindhoven University of Technology, P.O. Box 513, 5600 MB, Eindhoven, the Netherlands

ABSTRACT

Despite the enhancement of amorphous silica on Ultra-High Performance Concrete (UHPC), the influence of amorphous silicas on the mechanical contribution of coarse aggregates (CA) in UHPC from the perspective of multiscale is still unclear. Herein, the mechanical contribution of CA owing to the incorporation of silica with different morphology (i.e. nano-silica and silica fume) is studied from micromechanics to mesoscale fracture and macroscopic strength. The results show that, on the premise of guarantee flowability, silica fume generates more C–S–H but more microcracks owing to the higher content, while nano-silica results in a higher percentage of high-density C–S–H. The fracture across CA in pure tensile cracking is controlled by the competition between high-density C–S–H content and microcracks, whereas, the fracture across CA in pure shear cracking is governed by microstructure compactness. That is, the high-density C–S–H benefits more the fracture of CA in the case of tensile condition, while the microstructure compactness benefits more the fracture of CA in the case of shear condition. Consequently, in terms of the macroscopic strength, silica fume benefits more the mechanical contribution of CA in compressive loading because of the denser microstructure, while nano-silica is more beneficial to that in flexural loading owing to the higher content of high-density C–S–H.

1. Introduction

In spite of ultra-high strength, excellent ductility, and good durability, Ultra-High Performance Concrete (UHPC) exhibits a low sustainability, poor economic efficiency and high shrinkage cracking risk due to low water to binder ratio and high cement content [1–3]. To address these problems, researchers have proposed various kinds of methods [4–7], among which incorporating coarse aggregate (CA) into UHPC system to replace certain amount of cement has been proven to be an effective way [8–10]. According to the previous studies, the replacement of cement by CA not only improves the sustainability but also leads to a better volumetric stability and a higher elastic modulus [11–13]. Moreover, thanks to denser microstructure of UHPC-CA owing to low water/binder ratio, the fracture percentage of CA in UHPC-CA shows a higher level compared with normal concrete [14], suggesting the important role of CA in the mechanical performance of UHPC-CA. Given that CA is the hardest part in UHPC-CA [15,16], an in-depth

understanding of the mechanical contribution of CA is essential to the design and optimization of UHPC-CA.

Due to the "wall effect", CA disturbs the grain distribution in UHPC-CA, resulting in a weak zone, i.e., interfacial transition zone (ITZ) [17,18], leading to a heterogenous micromechanics. Our previous study indicates that, even though the microscale property of ITZ in UHPC is much better than that of normal concrete, ITZ is still the weakest part in UHPC-CA [18,19]. Because of the intrinsic weak characteristics, the appearance of ITZ aggravates the invasion risk of harmful substances [20,21]. To improve the micromechanical property of ITZ, amorphous silicas, such as nano-silica and silica fume, have been widely incorporated into UHPC, thanks to their pozzolanic effect and filler effect [22–24]. In the case of pozzolanic reaction effect, amorphous silica consumes portlandite and generates new calcium silicate hydrate (C–S–H) filling the microstructure [25–27]. Moreover, owing to the smaller size, nano-silica and silica fume not only fill the void space between cement particles, but also act as the nucleation surface of C–S–H,

---

promoting cement hydration reaction [28,29]. Combining the above advantages, the micromechanics of ITZ and matrix of UHPC-CA can be effectively improved simultaneously, thereby, improving the fracture proportion of CA, i.e., the mechanical contribution of CA in UHPC-CA.

Nevertheless, the cost of amorphous silica, especially nano-silica, is significantly higher than that of the rest raw materials of UHPC-CA. So, elucidating the role of amorphous silica on the improvement of mechanical contribution of CA in UHPC-CA and determining the proper dosage of amorphous silica are of great importance for the design and optimization of UHPC-CA. Many previous researches have been carried out to clarity the role of amorphous silica on the mechanical performance of UHPC without CA [30,31]. In terms of hydration reaction enhancement, some previous results suggest that nano-silica, with a higher surface area and a higher silanol content, exhibits a higher pozzolanic reactivity, while silica fume shows more obvious filler effect rather than pozzolanic effect [22,32]. In addition, compared to silica fume, the addition of nano-silica results in higher volume fraction of high-density C–S–H [33]. On the other hand, the incorporation of nano-silica and silica fume would also increase the autogenous shrinkage deformation of UHPC matrix, leading to a higher cracking risk of matrix [34–37]. Hence, it can be concluded that the incorporation of different kinds of amorphous silica would lead to different volume of cementation phase and microstructure, which is expected to alter the mechanical contribution of CA. In addition, owing to the spheric shape and lower specific surface area, a certain amount of silica fume shows positive effect to the flowability of UHPC [38]. In contrast, nano-silica has negative influence on the flowability of UHPC [39]. A worse flowability is expected to incorporate more air pore into UHPC matrix, which worsens the mechanical performance of UHPC-CA. Thus, flowability is a non-negligible parameter when determining the dosage of amorphous silica. Yet, the influence of different dosage of amorphous silica on the mechanical contribution of CA in UHPC-CA has not been well understood.

From the multiscale view, the macroscopic mechanical contribution of CA in UHPC-CA is resulted from the mesoscale fracture of CA, which is governed by the micromechanical property of UHPC-CA. Considering the different intrinsically different physical and chemical characteristics of nano-silica and silica fume, it is essential to understand micromechanical property, altered by the addition of nano-silica and silica fume, on the mechanical contribution of CA in UHPC-CA. From the perspective of fracture mechanics, the failure of concrete under compressive loading is mainly governed by shear cracking, while that under flexural loading is mainly governed by the tensile cracking [40,41]. Both denser microstructure and higher high-density C–S–H content are expected to enhance the mechanical contribution of CA in UHPC-CA [42,43]. Nonetheless, the influence of microstructure compactness and high-density C–S–H content on the shear fracture and tensile fracture of UHPC-CA has not been discussed separately. Moreover, microcracks due to the autogenous shrinkage could act as the weak part, providing the propagation path for the newly generated cracks [44]. That is, microcracks play a different role against denser microstructure and higher high-density C–S–H content. Hence, clarifying the influence of microstructure compactness, high-density C–S–H content and microcracks on the mechanical contribution of CA in UHPC-CA is of vital importance to the introducing of amorphous silicas into UHPC-CA. However, to date, the influence of the incorporation of amorphous silica on UHPC-CA, from micromechanics to mesoscale fracture and macroscopic strength, has not been well understood.

This study intends to clarify the influence of nano-silica and silica fume on the mechanical contribution of CA in UHPC-CA from a multiscale view. Firstly, the content of nano-silica and silica fume was determined based on the workability. The hydration products were characterized by TG and XRD, whereas microstructure compactness, high-density C–S–H content and microcracks were quantitatively analysed with the aid of scanning electron microscopy (SEM) and nano-indentation. Then, the mesoscale fracture characteristics of UHPC-CA

under pure tensile and pure shear fracture loading conditions were characterized quantitatively. The influence of micromechanical property on the mechanical contribution of CA in UHPC-CA was studied by comparing the macroscopic mechanical strength of UHPC-CA and UHPC. Finally, the transition of the mechanical contribution of CA in UHPC-CA because of the altered micromechanics by amorphous silica was discussed and the influencing mechanism of micromechanical distribution on the mechanical contribution of CA was revealed.

2. Materials and methods

2.1. Raw materials

Two kinds of amorphous silica, i.e., colloid nano-silica and silica fume, were used in this study. The Tecnai 20 microscope transmission electron microscope (TEM) was used to analyse the particle shape and particle size distribution of amorphous silica. As shown in Fig. 1(a) and (b), nano-silica particles show rough surface, whereas most of silica fume particles are spheric. Combining TEM and Image J, the particle size distribution of nano-silica and silica fume was quantified. As shown in Fig. 1(c), the particle size of nano-silica ranges from 0.005 to 0.02 μm, with a D50 of 0.01 μm, whereas that of silica fume ranges from 0.02 to 50 μm, with a D50 of 0.2 μm. In addition, the BET surface area of silica fume and nano-silica is 18.4 m^2/g and 160 m^2/g, respectively. The silanol content in nano-silica is 4–5 OH/nm^2, while that in silica fume is less than 1 OH/nm^2. The detailed chemical and physical properties of nano-silica and silica fume are presented in Table 1.

The other raw materials used in this study included Portland cement CEM I 52.5R, fine quartz sand 0–0.2 mm, normal sand 0–2 mm, basalt aggregate 2–5 mm and 5–8 mm, tap water (W), and polycarboxylate-type superplasticizer containing solid content of 35% (SP). The chemical and physical properties of Portland cement is shown in Table 1. The particle size distribution of the raw materials is presented in Fig. 2. Herein, to eliminate the influence of steel fiber on the mechanical performance of UHPC-CA, the steel fiber was not incorporated in UHPC-CA system.

2.2. Mix design of UHPC and UHPC-CA

In this study, to investigate the mechanical contribution of CA, both UHPC and UHPC-CA were designed. The recipe of reference sample, including UHPC and UHPC-CA, is presented in Table 2. 30% volume content of CA was used in UHPC-CA. The water to binder ratio (w/b) was set as 0.2. To study the influence of amorphous silica on the workability of UHPC, based on the preliminary study, the cement was substituted by 1%, 2%, 3%, 4%, 5% of nano-silica and 5%, 10%, 15%, 20% and 25% of silica fume, respectively. Noting that the nano-silica used in this study is firstly dispersed in a solution to avoid agglomeration.

Due to that the high surface area of amorphous silica absorbs high amount of water, flowability of UHPC is worsened in the case of excessive amorphous silica. It would entrap extra air into the fresh mixture, resulting in a higher porosity due to the reduced flowability and increased viscosity [38,39]. Thus, considering the workability, a proper content of amorphous silica should be determined. To determine the proper substitution of cement by nano-silica and silica fume, the mini slump flow method was used to characterize the influence of amorphous silica on the flowability of UHPC mortar. More detailed information of the measurement procedure can be found in Ref. [45]. The contents of water and superplasticizer were kept constant.

2.3. Specimen preparation

All the samples were cured in water and the temperature was kept as 25 °C. The total curing age was set as 28 days. More detailed information about casting and curing procedure can be found in Refs. [9,46]. Three
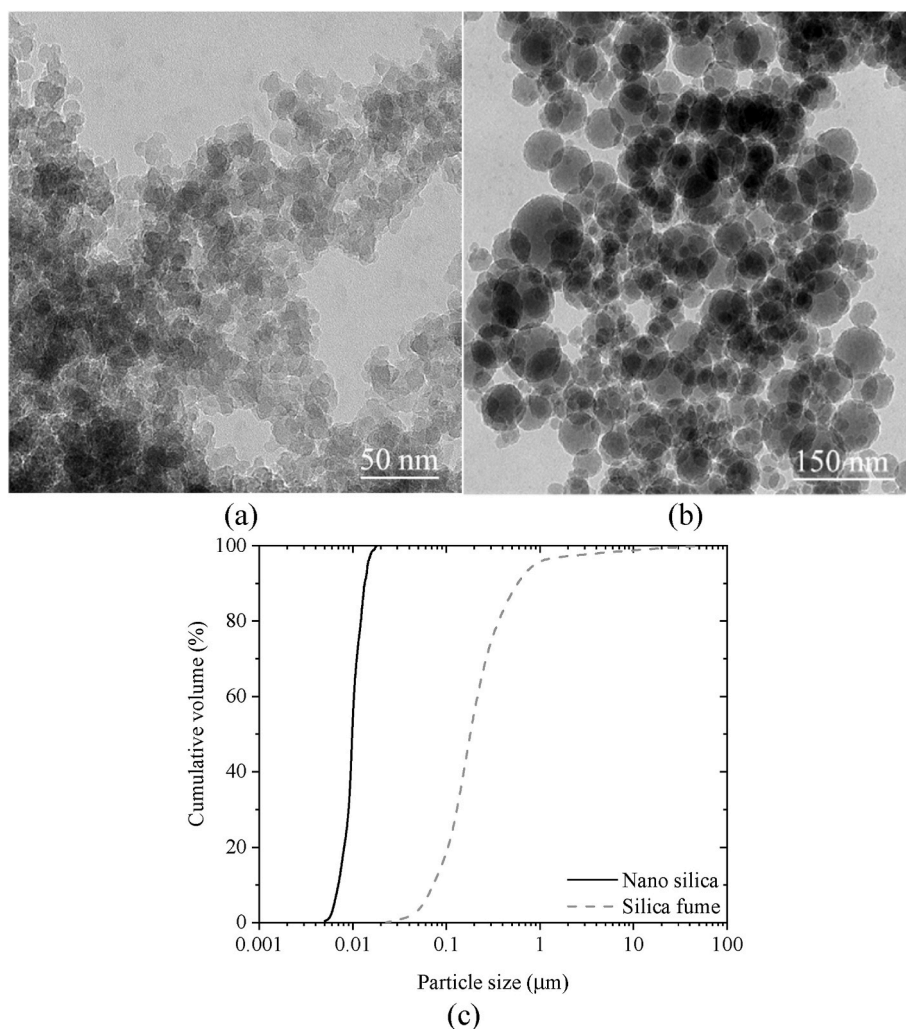
Fig. 1. TEM images and particle size distribution of nano-silica and silica fume. (a) TEM image of nano-silica; (b) TEM image of silica fume; (c) Particle size distribution of nano-silica and silica fume.

Table 1
Chemical and physical properties of PC, SF and NS.

Substituent (%)	PC	SF	NS
CaO	64.60	0.90	0.089
SiO$_2$	20.08	93.06	98.68
Al$_2$O$_3$	4.98	—	0.367
Fe$_2$O$_3$	3.24	2.06	0.004
K$_2$O	0.53	1.15	0.354
Na$_2$O	0.27	0.63	0.315
SO$_3$	3.13	1.28	—
MgO	1.98	0.70	—
TiO$_2$	0.30	—	0.007
MnO	0.10	0.07	—
LOI (1000 °C)	0.51	0.88	—
BET surface area (m^2/g)	1.004	18.4	160
Specific density (g/cm^3)	3.15	2.20	2.2

different kinds of samples were produced for mechanical test. In addition, cylinder sample with a diameter of 100 mm and height of 200 mm was used for producing sample for fracture test, while cubic sample with $50 \times 50 \times 50$ mm^3 was used for compressive strength and prism sample with $40 \times 40 \times 160$ mm^3 was used for flexural strength. The dimensions of all samples are at least 5 times of the maximum size of CA.

To analyse the influence of amorphous silica on the mesoscale fracture of UHPC-CA under different stress condition, the fracture tests of UHPC-CA under pure I and II fracture conditions, i.e., pure tensile

fracture and pure shear fracture, were carried out. Instead of the traditional short, which can't get the pure shear fracture condition, half-circular disk specimen with a straight notch was used for the fracture test. As shown in Fig. 3, the notch with an inclination angle of 0° was used for pure I, whereas the notch with an inclination angle of 54° was used for pure II fracture [47]. The crack length is 17 mm.

2.4. Methodology

2.4.1. Hydration products analysis

To analyse the influence of amorphous silica on the hydration products, the X-ray diffraction (XRD) and thermal gravity (TG) analysis of paste sample with 28 days curing age were carried out. All the samples for hydration products analysis were firstly broken into small pieces and immersed into isopropanol to terminate hydration. Then, the samples were dried in a vacuum oven at 60 °C for 24 h and grounded into powder with the size less than 80 μm. XRD analysis was carried out by a Bruker D4 phaser instrument. The parameters were set as time 0.6 s, with the increment of 0.02, scanning range from 10° to 70°. The TG analysis was conducted using a STA 449C F1 instrument. The heating rate during this measurement was 10 °C/min, from 20 °C to 1000 °C under nitrogen flow.

2.4.2. Quantitative characterization of microstructure

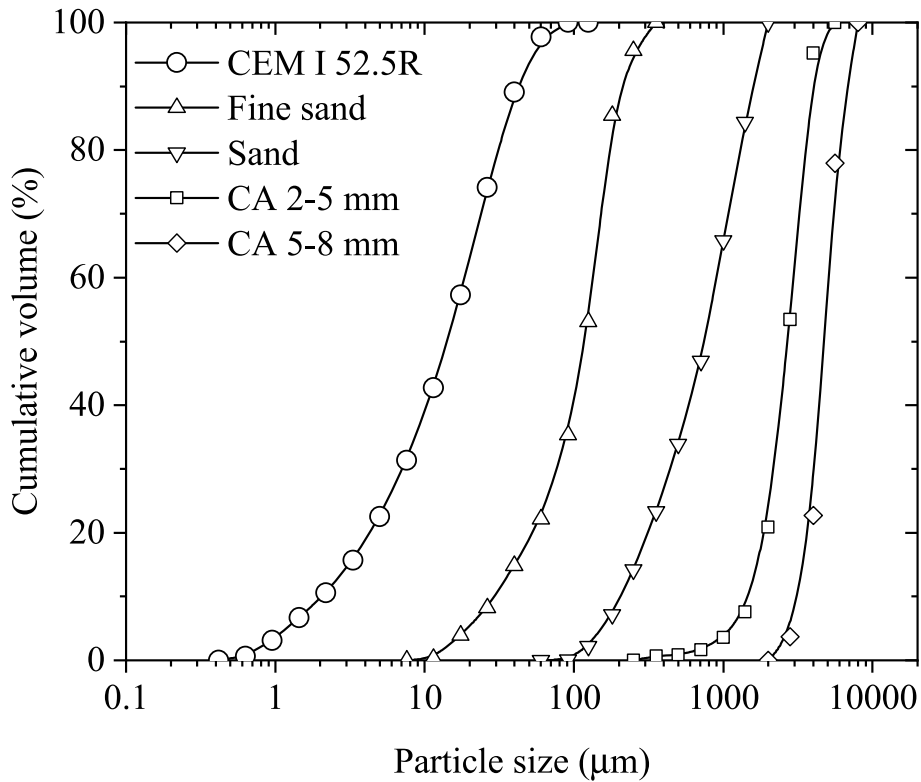To quantitatively characterize the influence of amorphous silica on

Fig. 2. Particle size of raw materials for UHPC-CA.

Table 2
Mix design of UHPC and UHPC-CA.

	CEM (kg/m^3)	Fine sand (kg/m^3)	Sand (kg/m^3)	CA 2–5 (kg/m^3)	CA 5–8 (kg/m^3)	Water (kg/m^3)	SP (kg/m^3)
UHPC	820.82	145.24	831.65	0	0	141.29	35.18
UHPC-CA	615.62	108.93	623.74	400	200	105.97	26.38

the microstructure of UHPC-CA, the combination of SEM equipped with a backscattered electron (BSEM) and quantitative image process method was used in this study. To ensure the statistical significance, 5 samples were prepared and 10 areas were observed randomly in each sample. Concentric expansion method was used for the quantitative analysis of porosity of the zone along CA boundary [48,49]. Considering that the width of ITZ is around 40 μm–50 μm [18], 7 successive strips with a spacing 10 μm, which can cover the whole ITZ, was analysed.

Meanwhile, to quantify the microcracks in UHPC-CA, an image process based on the gray of image was used. The processing procedure includes filtering, segmentation, skeletonization and microcracks length calculation. Noting that the gray threshold of microcracks or micropores is determined based on the tangent-slope method. More information concerning the image process method can be found in our previous study [50]. The lengths of microcracks are determined based on the gray distribution of the BSEM images. To quantify the microcracks distribution, the cracks density was calculated as follows:

$$\rho = \frac{L}{A} \tag{1}$$

where L is the total length of microcracks and A is the area of the observation region.

2.4.3. Quantitative characterization of micromechanical property

To analyse the influence of amorphous silica on the micromechanical property of UHPC-CA. Nano-indentation test in the area along the boundary of CA was carried out. A Hysitron Ti950 Triboindenter and a Berkovich indenter were used in the test, in which a trapezoidal loading style was utilized. More detailed information of the loading condition can be found in Ref. [51]. As shown in Fig. 4, a 10×10 indentation grid with indent spacing of 10 μm was used to get enough data to fulfil the
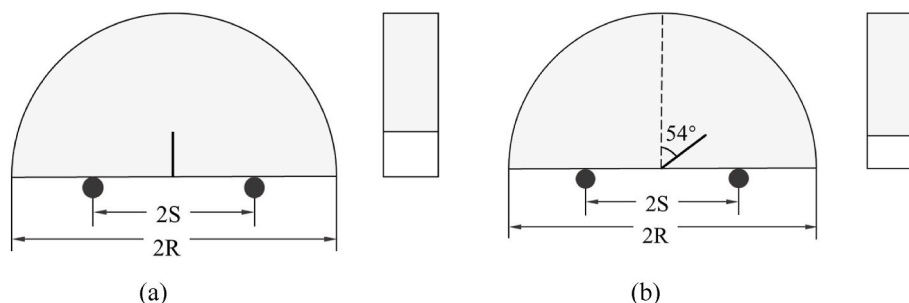

Fig. 3. The schematic diagram of notched half disk specimen used for fracture test. (a) Pure I fracture; (b) Pure II fracture.

statistical significance. The elastic modulus *E* was calculated based on the Oliver-Pharr method [52]. To further quantify the hydration products owing to the addition of amorphous silica, the data from nano-indentation test were deconvoluted based on the gaussian function. The percentage of each phase in ITZ along CA was calculated based on probability density function from deconvolution process [53,54].

2.4.4. Quantitative characterization of mesoscale fracture of UHPC-CA

To analyse the mesoscale fracture characteristics of UHPC-CA, three points bending test was selected as the loading type, where the span (2*S*) is 50 mm. The fracture energy was calculated based on the loading force-deflection curve. The fracture percentage of CA, ITZ and matrix of UHPC-CA, was quantified, respectively. Herein, an image processing method proposed by the authors was used. In this method, a CA grain is assumed to be fractured if a "mirrored" CA grain appears in the same position on the two fracture surfaces. More detailed information of this method can be found in the previous research [14,19].

2.4.5. Compressive strength and flexural strength

The compressive strength and flexural strength of UHPC-CA were tested after 28 days curing age. The cubic sample with size of 50 mm × 50 mm × 50 mm was used for compressive test, whereas the prism sample with size of 40 mm × 40 mm × 160 mm was used for flexural test. The loading rate of the compressive test is 5 kN/s, whereas the that of the flexural test is 0.2 mm/min. The average strength values were obtained from three parallel samples.

3. Results and discussion

3.1. Flowability of fresh UHPC

The mini slump flowability of fresh UHPC mortar was measured to determine the proper addition of nano-silica and silica fume. As shown in Fig. 5 (a), the rest results indicate that the flowability decreases with the increase of nano-silica addition, especially, there is an obvious decrease of flowability as the nano-silica addition is higher than 3%. It could be attributed to the high surface area of nano-silica, resulting in that more water is needed to achieve a good workability with the addition of nano-silica [39]. However, as shown in Fig. 5 (b), in the case of silica fume, there is a turning point in the case of 5% addition of silica fume, lower than which the incorporation of silica fume has a positive

Fig. 4. Indentation grid of nanoindentation test.

effect on the flowability, in contrast, higher than which the flowability decreases with the increase of silica fume. The turning phenomenon is consistent with the previous study [38]. The improvement effect of silica fume has been assigned to its sphere shape, which shows the lubrication effect [38,55]. On the other hand, the worse flow in the case of too high addition silica can be related to the high surface area of silica fume, which has been reported in the previous study [56]. Normally, the entrapped air increases with the increase of viscosity due to the low workability. According to the previous study [39], the optimal silica amount should be controlled as the flowability is higher than 250 mm. Otherwise, the positive effect of amorphous silica would be compromised significantly by the increased porosity assigned to the entrapped air. Hence, in this study, the maximum addition of nano-silica was recommended as 3%, while that of silica fume was recommended as 15%.

3.2. Hydration products

Both the pozzolanic reaction and filler effect of amorphous silica promote the generation of C–S–H, which is primarily responsible for the strength of UHPC. As shown in Fig. 6 (a) and Fig. 6 (b), portlandite can still be observed in the sample with 15% silica fume, which implies that not all the amorphous silica is consumed for pozzolanic reaction, which is consistent with the previous researches [22,57]. To quantitatively analyse the influence of different amorphous silica on the hydration products of UHPC, the water content in C–S–H is calculated. As shown in Fig. 6 (c), compared with the reference sample, the bound water in C–S–H increases with the increased content of both nano silica and silica fume. It is noteworthy that the bound water in the sample with 3% nano-silica, i.e. 7.9%, is lower than that in the sample with 15% silica fume i.e. 8.2%. This could be attributed to the high volume of silica fume, part of which act as seeding surface [22], even though some of silica fume does not react with portlandite due to the low pozzolanic reactivity. However, the bound water in the sample with 3% nano-silica is higher than that in sample with 5% silica fume. This confirms that the hydration promotion effect of nano-silica is better than silica fume, which is in line with the previous research [58–60].

3.3. Microscale characteristics

3.3.1. Microstructure

To investigate the influence of amorphous silica on the microstructure of UHPC-CA, the BSEM images of UHPC-CA are presented. As shown in Fig. 7, the microstructure of UHPC-CA with nano-silica and silica fume is denser than that of the sample without amorphous silica, in which some obvious defects can be found. The denser microstructure could be attributed to the combination of pozzolanic and filler effect of amorphous silica, which generate more C–S–H filling the initial defects. In addition, owing to the higher content of silica fume, the microstructure of sample with 15% silica fume is better than that of the sample with 3% nano-silica, which is consistent with the TG results. However, compared with the sample containing 3% nano-silica, more microcracks with aperture less than 1 μm can be observed in the sample with 15% silica fume. The higher content of microcracks could be related to the higher content of silica fume, which is capable of refining the capillary pores and intensifying the relative humidity decrease, thereby increasing the autogenous shrinkage deformation [61–63].

To quantitively analyse the influence of amorphous silica on the microstructure of UHPC-CA, the porosity along CA is presented in Fig. 8. As shown in the result of the sample without amorphous silica, the porosity decreases with the increase of distance from CA boundary till to about 20~30 μm, suggesting the existence and range of ITZ, which has been assigned to the so-called "wall" effect disrupting the packing of cement grains against the CA [64]. Noteworthy, the width of the ITZ in reference sample is obviously less than that of normal concrete, which is normally around 40 ~50 μm [18]. It should be related to the low water
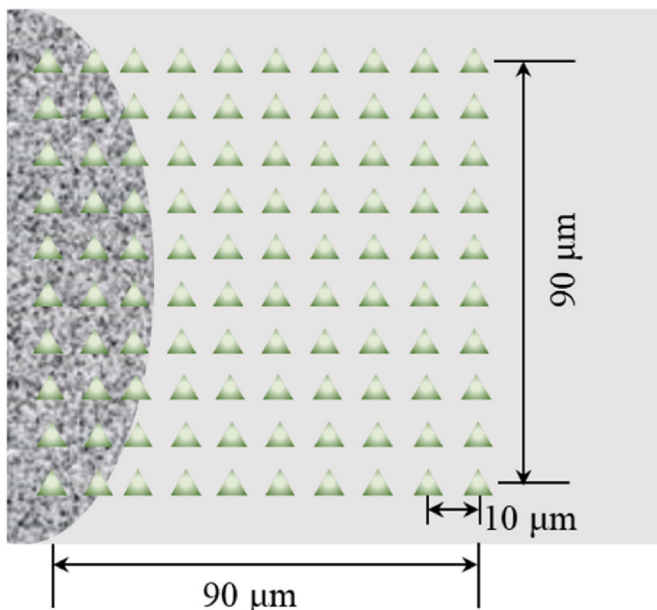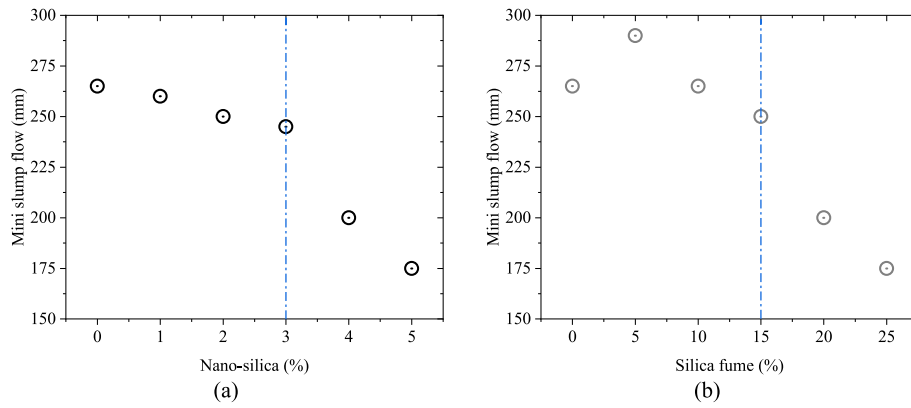
Fig. 5. The mini slump flow of fresh UHPC with different amorphous silica. (a) Nano-silica; (b) Silica fume.
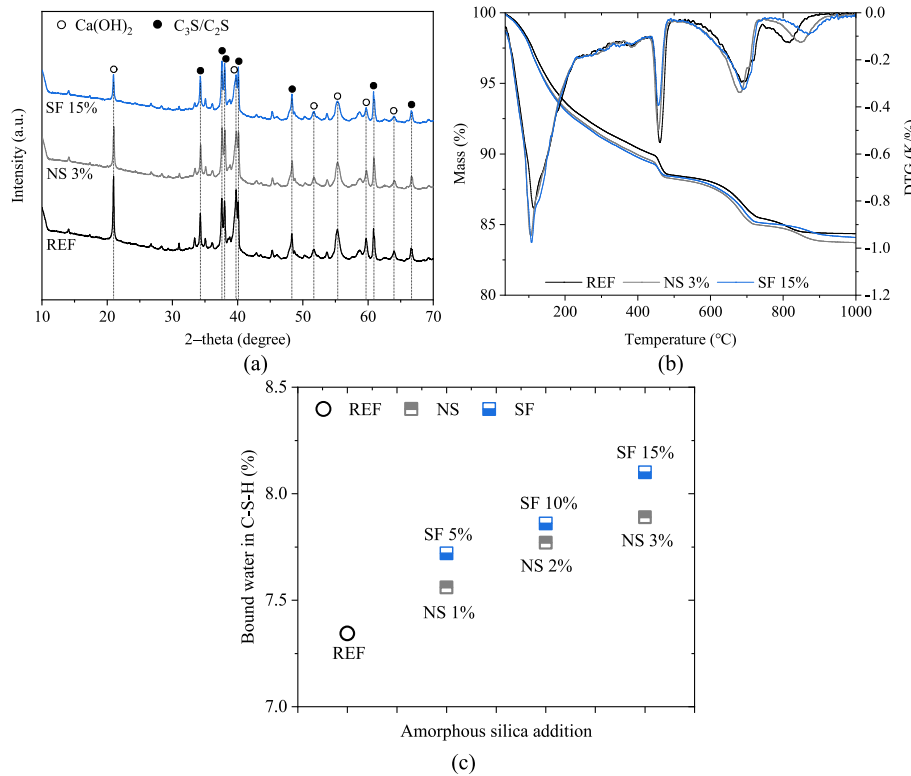

Fig. 6. The hydration products of UHPC with different amorphous silica. (a) XRD pattern; (b) TG-mass; (c) Bond water in C–S–H. (REF: sample without amorphous silica; NS: sample with nano-silica; SF: sample with silica fume.)

to cement ratio in UHPC-CA, which densifies the microstructure of ITZ [65,66]. With the addition of nano-silica and silica fume, the porosity shows a decreasing trend, which can be attributed to the higher C–S–H content in the case of amorphous silica. It further confirms the positive effect of amorphous silica on densifying microstructure of UHCP-CA.

To further quantify the influence of amorphous silica on the microstructure of UHPC-CA matrix, the size of pores and porosity of matrix of UHPC-CA are shown in Fig. 8 (c) and (d). As shown in Fig. 8 (c), with the addition of amorphous silica, the diameter of pores in UHPC matrix tends to be smaller, which suggests that nano-silica and silica fume can optimize pore structure. Moreover, the pore size in UHPC-CA containing silica fume is smaller than that in UHPC-CA containing nano-silica. In addition, as shown in Fig. 8 (d), the porosity of the sample with 3% nano-silica is higher than that of the sample with 15% silica fume. These suggest the greater contribution to densify the microstructure from silica fume. This could be attributed to the higher content of silica fume, which

fills the initial defects of UHPC-CA. However, the porosity of the sample with 3% nano-silica is lower than that of the sample with 5% silica fume. This indicates that nano-silica has higher reactivity than silica fume, which is consistent with the previous studies [22,33].

Considering the increasing shrinkage deformation due to the addition of amorphous silica, the average length of microcracks in UHPC-CA and the linear crack density of sample with amorphous silica is presented in Fig. 9 to clarify the influence of amorphous silica on the microcracks in UHPC-CA. As shown in Fig. 9 (a), with the addition of amorphous silica, the average length of microcracks in UHPC-CA shows an increasing tendency. Meanwhile, as shown in Fig. 9 (b) and (c), the linear crack density of the sample without amorphous silica is 0.024 μm/μm², which shows a higher level with the addition of amorphous silica. It can be attributed to the higher shrinkage deformation due to the addition of amorphous silica [36]. Specifically, the linear crack density increases to 0.028, 0.031 and 0.038 μm/μm² in the case of the nano-silica
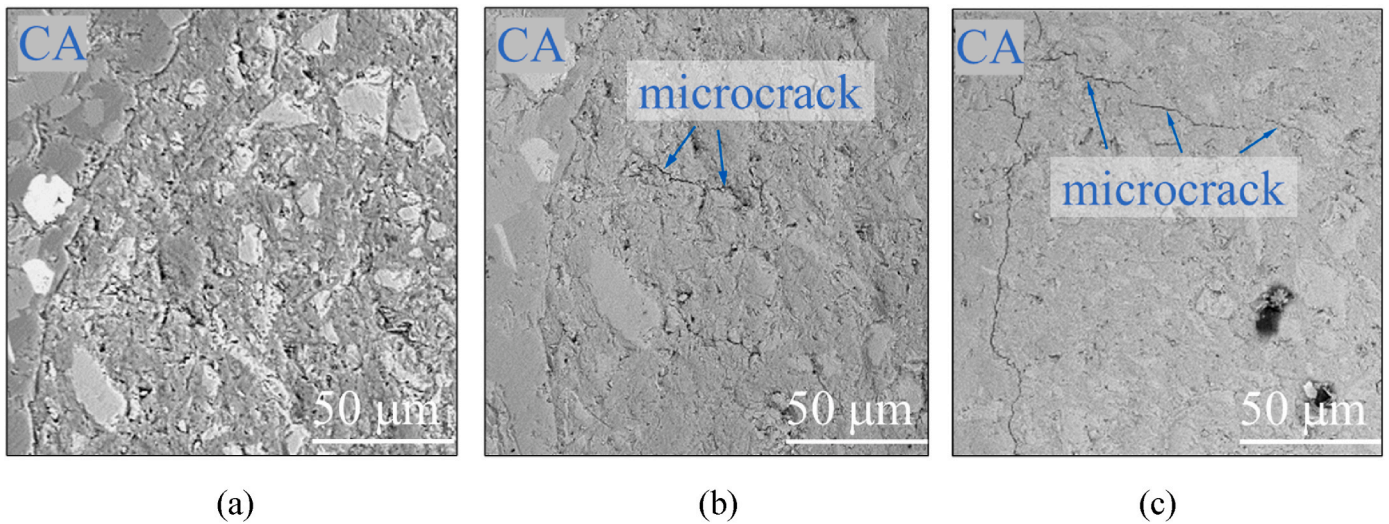
Fig. 7. Microstructure of UHPC-CA containing amorphous silica. (a) Sample without amorphous silica; (b) Sample with 3% nano-silica; (c) Sample with 15% silica fume.
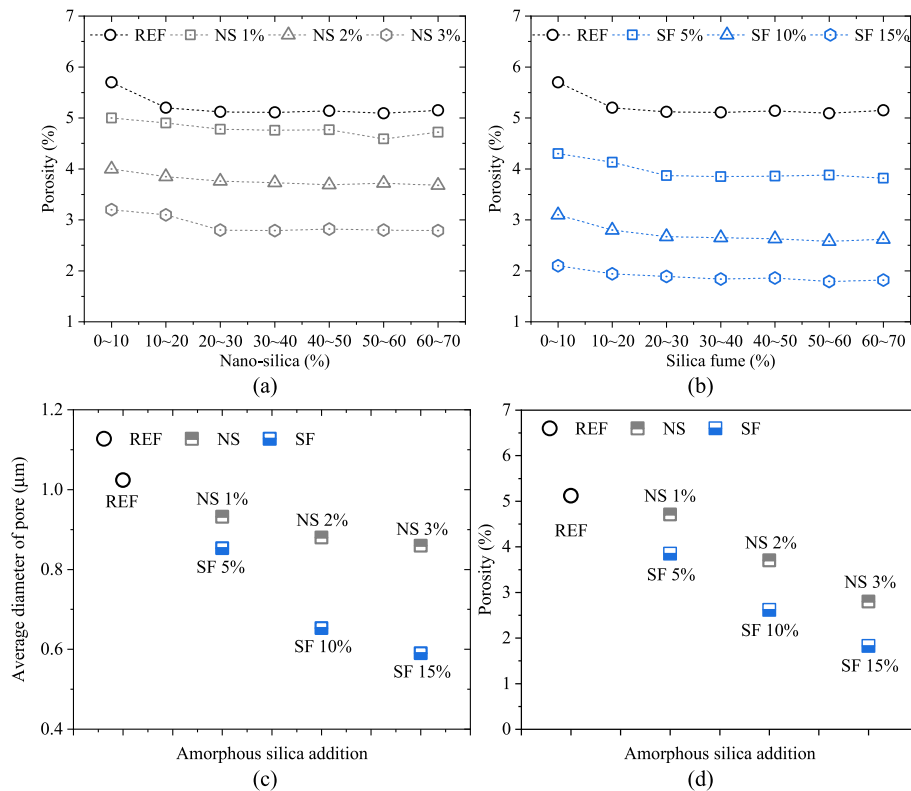

Fig. 8. Porosity of UHPC-CA containing amorphous silica. (a) UHPC-CA with nano-silica; (b) UHPC-CA with silica fume; (c) Average diameter of porosity in UHPC matrix; (d) Porosity of UHPC matrix. (REF: sample without amorphous silica; NS: sample with nano-silica; SF: sample with silica fume.)

addition of 1%, 2% and 3%, respectively. Meanwhile, the linear crack density increases to 0.032, 0.044 and 0.087 μm/μm² in the case of the silica fume addition of 5%, 10% and 15%, respectively. It is noteworthy that the sample with silica fume contains more microcracks than that with nano-silica. This could be attributed to two reasons: the first one is that a higher content of silica fume results in a larger humidity decrease, and the second one is that a denser microstructure, owing to the filling effect of silica fume, leads to a higher capillary force [67]. The combination of these two factors results in a higher shrinkage deformation, consequently, more potential microcracks.

3.3.2. Micromechanics property

To analyse the influence of amorphous silica on the micromechanical property of UHPC-CA, the elastic modulus along the boundary of CA is characterized. The contour map of the elastic modulus of UHPC-CA is presented in Fig. 10 (a). It is observed that the CA part shows the highest elastic modulus, which suggests that the fracture of CA would contribute to more mechanical strength of UHPC-CA [14]. Meanwhile, the part without CA exhibits obvious heterogeneity, which can be attributed to the content of low density C–S–H, high density C–S–H, portlandite, ultra-high density C–S–H and un-hydrated cement particles. It is
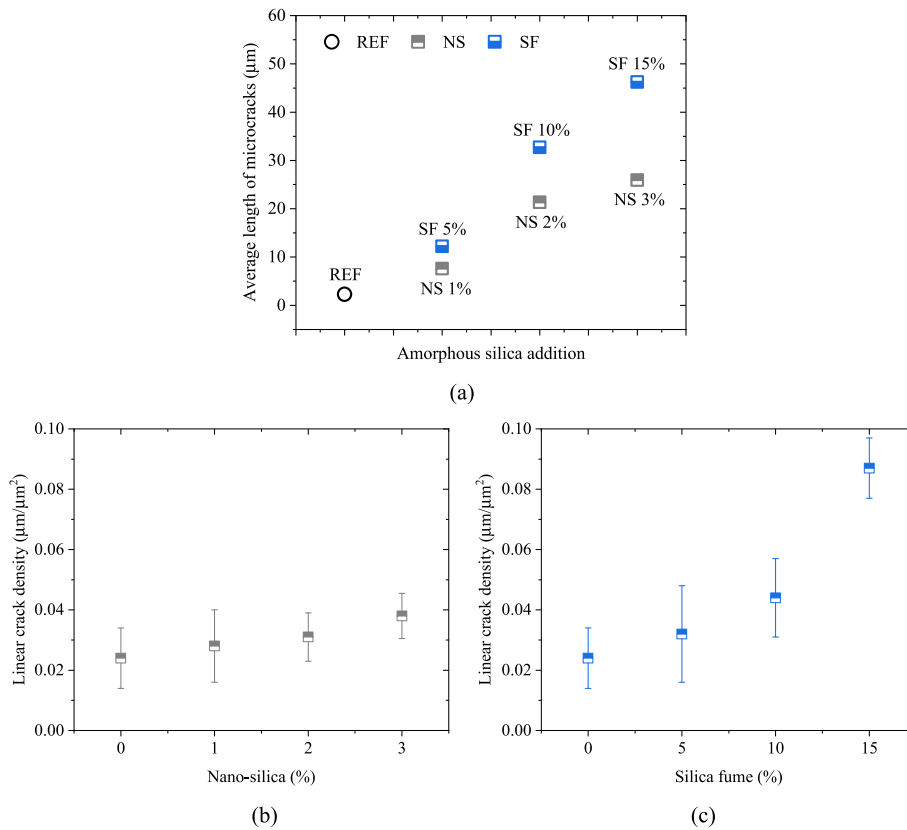

pozzolanic reaction and seeding effect, both nano-silica and silica fume have positive effect on the total content of C–S–H, including low density C–S–H and high density C–S–H. For example, the total C–S–H content, including low density C–S–H and high density C–S–H, in the reference sample is 42.2%, whereas that of sample with 3% nano-silica and silica fume is 59.3% and 63.5%, respectively. However, the C–S–H in the sample with 3% nano-silica, i.e. 60%, is higher than that of sample with 5% silica fume, i.e. 50%, suggesting a higher reactivity of nano-silica compared to silica fume. It is noted that the above results agree well with the TG results. A higher content of C–S–H is expected to result in a denser microstructure, which can be confirmed by the quantitative microstructure result from SEM. In addition, as shown in Fig. 11 (c), the relative proportion of high density C–S–H in the sample with 1%, 2% and 3% nano-silica is higher than that in the sample with 5%, 10% and 15% silica fume, respectively. It could be attributed to the high surface area of nano-silica, which provides more seeding point for C–S–H [33].

3.4. Fracture characteristics of UHPC-CA

The fracture energy of UHPC and UHPC-CA are presented in Fig. 12 to analyse the influence of amorphous silica on the fracture performance of UHPC and UHPC-CA. In the case of the sample without amorphous silica, the pure tensile fracture energy of UHPC-CA is lower than that of UHPC. In contrast, the pure shear fracture energy of UHPC-CA is higher than that of UHPC. It is suggested that the role of CA in UHPC-CA changes with the loading condition. Moreover, the influence of amorphous silica on the pure tensile fracture energy of UHPC-CA evolves with the silica type and content. For example, as shown in Fig. 12 (a), in the case of nano-silica, the pure tensile fracture energy of UHPC is larger than that of UHPC-CA as the content is lower than 2%, whereas the pure tensile facture energy of UHPC becomes lower than that of UHPC-CA as the content reaches to 3%. However, as shown in Fig. 12 (c), in the case

of silica fume, the pure tensile fracture energy of UHPC remains higher than that of UHPC-CA. In addition, as shown in Fig. 12 (b) and (d), despite the type and content of amorphous silica, the pure shear fracture energy of UHPC-CA is higher than that of UHPC, which suggests the positive contribution of CA on the fracture performance of UHPC-CA. Given the different microstructure and micromechanics of UHPC-CA owing to the contain of amorphous silica, the role of CA in the fracture energy of UHPC-CA could be related to the microscale property and the loading condition.

3.5. Mesoscale fracture characteristics of UHPC-CA

To analyse the influence of amorphous silica on the mesoscale fracture characteristics of UHPC-CA, the fracture percentage of matrix, ITZ and CA was quantified based on the image process method. As shown in Fig. 13, despite the loading condition and the amorphous silica content, the fracture across CA can be found, indicating the mechanical contribution potential from CA. It is different with the normal concrete, in which the mechanical contribution from CA can be barely found due to the weaker ITZ compared to UHPC [72–74]. Besides, in the case of the pure tensile fracture loading condition, i.e., the pure tensile cracking, the fracture across CA increases with nano-silica content, from 1% to 3%. In contrast, the fracture across CA shows the highest value as silica fume addition is 10%, which then decreases as the silica fume addition further increases. It could be related to the microstructure and micromechanical property altered by the addition nano-silica and silica fume.

In addition, in the case of the pure shear fracture loading condition, the fracture across CA increases with increasing amorphous silica addition, regardless of the type of amorphous silica. In addition, compared with fracture percentage of CA in the pure tensile fracture loading condition, it can be observed that the fracture across CA in the pure shear fracture loading condition shows a higher level, suggesting a
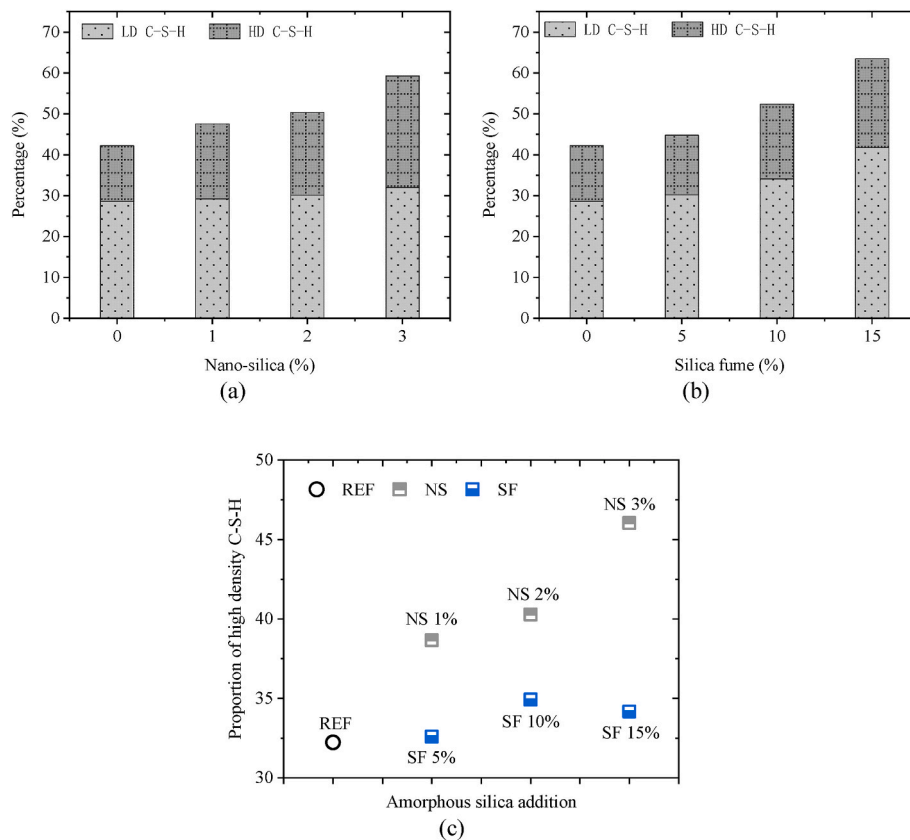

Fig. 11. Quantification of low density C–S–H and high density C–S–H in UHPC. (a) Sample with nano-silica; (b) Sample with silica fume; (c) The proportion of high density C–S–H in the total C–S–H. (REF: sample without amorphous silica; NS: sample with nano-silica; SF: sample with silica fume.)
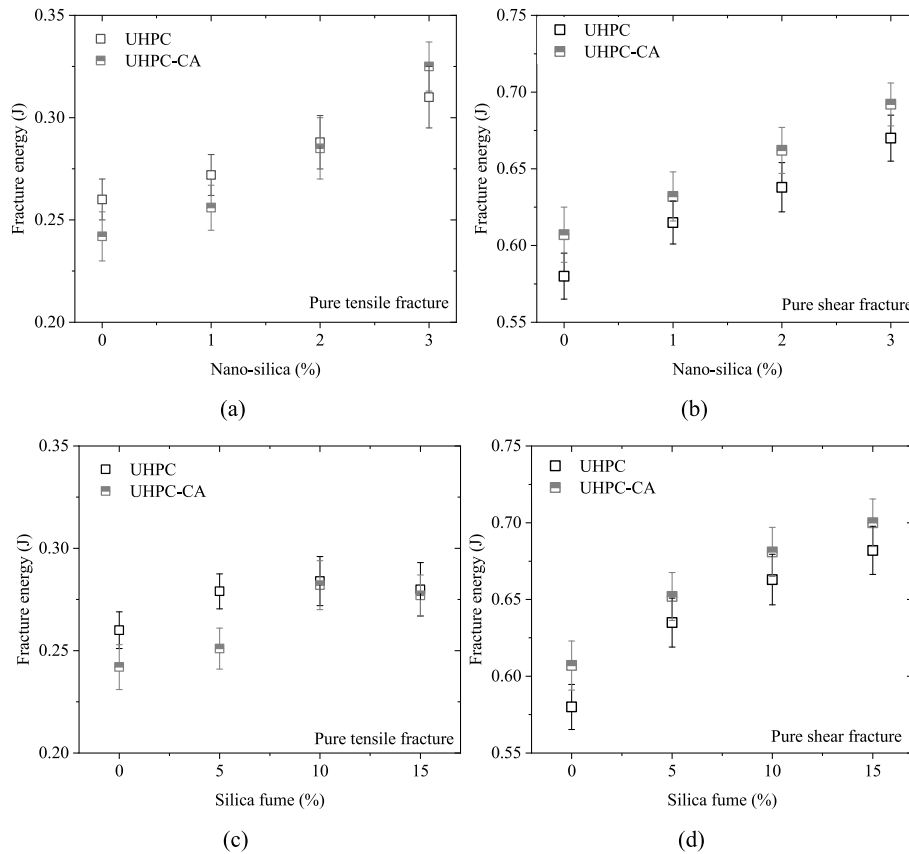
Fig. 12. Fracture energy of UHPC and UHPC-CA. (a) Sample containing nano-silica under fracture I; (b) Sample containing nano-silica under fracture II; (c) Sample containing silica fume under fracture I; (d) Sample containing silica fume under fracture II.

higher mechanical contribution of CA in shear fracture condition. It could be attributed to the more important role of interlock from CA in the shear fracture loading condition, which leads to a higher stress concentration around CA, in consequence, a higher fracture percentage of CA. The evolution of fracture percentage of CA suggests that the mechanical contribution from CA is not only controlled by the micromechanical property of UHPC, but also varies with the cracking condition.

3.6. Compressive strength and flexural strength

The compressive strength and flexural strength of UHPC and UHPC-CA are presented in Fig. 14 to analyse the influence of amorphous silica on the macroscopic mechanical contribution of CA in UHPC-CA. In the case of the sample without amorphous silica, the compressive strength of UHPC-CA is higher than that of UHPC. In contrast, the flexural strength of UHPC-CA is lower than that of UHPC, which is in line with the previous studies [15,75]. This implies that CA plays very different roles in UHPC-CA under different loading conditions, which could be attributed to that different loading conditions result in different stress conditions around CA. The difference could be related to the presence of ITZ, which is the weakest part in UHPC-CA as shown in Fig. 10, owing to the incorporation of CA.

Despite of the type and content of amorphous silica, the compressive strength of UHPC-CA is higher than that of UHPC, which means that the mechanical contribution of CA is positive in the case of the compressive loading condition. However, the flexural strength of UHPC-CA is higher than that of UHPC when the nano-silica content is higher than 1%, whereas, in the case of silica fume, the flexural strength of UHPC-CA is constantly lower than that of UHPC despite of the content of silica fume. It could be assigned to that the nano-silica results in a higher content of

high-density C–S–H, which is more beneficial to the bonding property of CA. It is suggested that the microstructure and micromechanical properties govern the mechanical contribution of CA in the macroscopic mechanical strength of UHPC-CA. Noting that both of the flexural strengths of UHPC and UHPC-CA show no obvious variation as the silica fume increases from 10% to 15%, which could be attributed to the increase of microcracks related to the higher autogenous shrinkage deformation, as shown in Fig. 7 (c).

4. Discussion

From the perspective of multiscale, the failure of concrete under compressive loading can be attributed to the shear cracking, whereas that under flexural loading is related to the tensile cracking. To clarify the influence of amorphous silica on the mechanical contribution of CA in UHPC-CA, the governing mechanism of microstructure compactness, percentage of high-density C–S–H and microcracks on the fracture of UHPC-CA under tensile and shear cracking should be elucidated. Thus, the influence of amorphous silica on the micromechanical characteristics, i.e., microstructure compactness, percentage of high-density C–S–H and microcracks, of UHPC-CA is firstly discussed based on the hydration products, BSEM and nano-indentation results. Then, the effect of micromechanics on the mesoscale fracture of UHPC-CA is clarified to deepen our understanding on the influence of amorphous silica on the macroscopic mechanical contribution of CA in UHPC-CA.

4.1. Influence of amorphous silica on the micromechanics of UHPC-CA

It has been widely acknowledged that the hydration enhancement of silica fume is weaker than that of nano-silica. It can also be confirmed by that the C–S–H content of sample with 3% nano-silica is higher than that
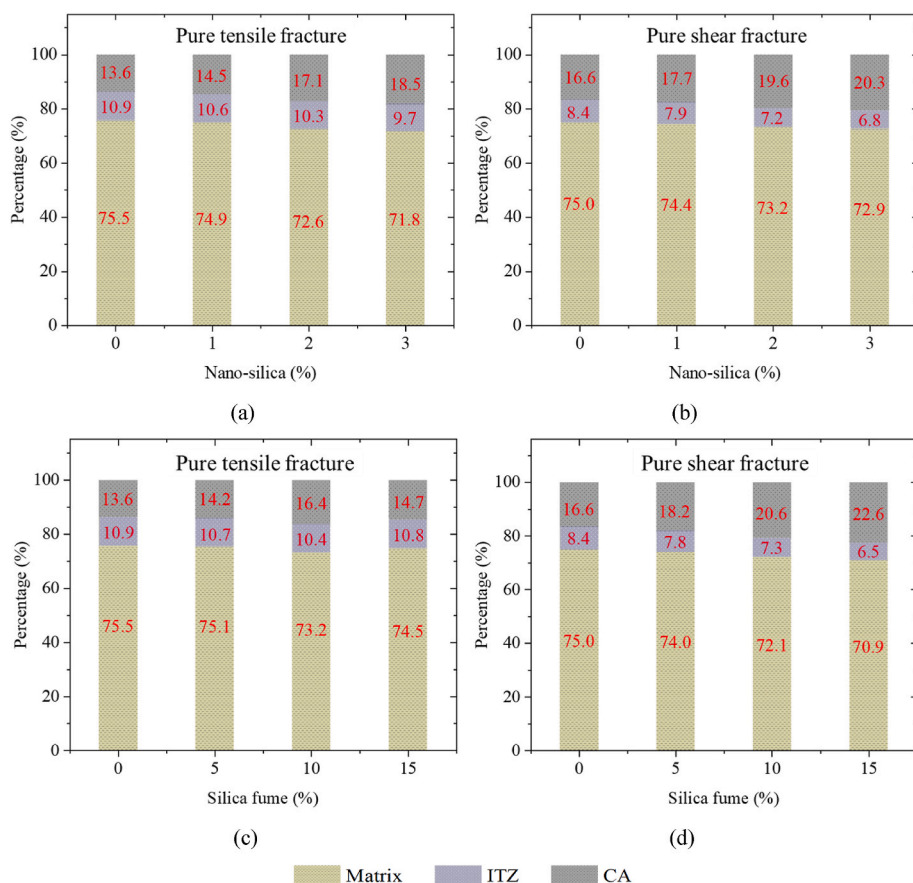
Fig. 13. Mesoscale fracture percentage of matrix, ITZ and CA. (a) UHPC-CA containing nano-silica under fracture I; (b) UHPC-CA containing nano-silica under fracture II; (c) UHPC-CA containing silica fume under fracture I; (d) UHPC-CA containing silica fume under fracture II.

of the sample with 5% silica fume. However, owing to the spherical shape and the lower specific surface area, the content of silica fume is higher than that of nano-silica considering the flowability of UHPC. Most of the research just discussed the hydration products and microstructure of UHPC containing same amorphous silica. In contrast, in this study, the silica fume content is higher than that of nano-silica. Due to the higher maximum content of silica fume, the bound water in C–S–H of the sample with 3% nano-silica is lower than that of the sample with 15% silica fume. Consequently, the microstructure of sample with 15% silica fume is denser than that of sample with 3% nano-silica.

The sample with silica fume exhibits a higher pozzolanic reaction, which can be proved by the lower portlandite content and higher C–S–H content in the sample with 15% silica fume compared to that with 3% nano-silica. The previous study suggests that the pozzolanic effect results in a higher chemical volume reduction, which is expected to increase the autogenous shrinkage deformation [34]. In addition, as the sample with silica fume shows a denser microstructure, a given chemical shrinkage would lead to a more vigorous self-desiccation in a finer pore than in a coarser pore. Meanwhile, as the high density C–S–H content in sample with nano-silica is higher than that in sample with silica fume, the higher autogenous shrinkage is expected to result in more microcracks. To further clarify the influence of nano-silica and silica fume on the micromechanical property of UHPC-CA, a schematic diagram of UHPC-CA containing amorphous silica is presented in Fig. 15.

As shown in Fig. 15 (a), due to the so called "wall" effect, there is a transition zone along CA, which is the weakest part of UHPC-CA. Normally, the width of ITZ is around 40 μm–50 μm in normal concrete [18]. Owing to the ultra-low water to cement ratio in this study, i.e. 0.2, the ITZ is significantly reduced, to less than 10 μm, even without amorphous silica. This has also been observed in our previous study [19]. Thanks to

that both of the particle size of nano-silica and silica fume are smaller than that of cement particle, ITZ can be refined by nano-silica and silica fume. In addition, the portlandite can be consumed by pozzolanic reaction, which results in more C–S–H filling the pores along CA boundary. Combining the filler effect and pozzolanic effect of nano-silica and silica fume, the microstructure of ITZ is densified. Hence, in the case of the sample containing 3% nano-silica and 15% silica fume, the ITZ is almost negligible, as shown in Fig. 15 (b) and (c). Due to the higher maximum content of silica fume, the microstructure of sample with 15% silica fume, as shown in Fig. 15 (c), is denser than that of sample with 3% nano-silica, as shown in Fig. 15 (b). Moreover, since the surface area and silanol content of nano-silica is higher than that of silica fume, the proportion of high-density C–S–H, which is not accessible for N_2, in sample with 3% nano-silica is higher than that of silica fume [76], as shown in Fig. 11. It is beneficial for the improvement of the bonding property between CA and ITZ in the sample with nano-silica.

It can be concluded that, thanks to the higher content, silica fume generates more C–S–H, resulting in a denser microstructure despite of the lower hydration improvement compared to nano-silica. However, the higher content of silica fume leads to a higher shrinkage induced microcracks in UHPC matrix. Hence, besides the flowability, it should be kept in mind that the incorporation of silica fume should be controlled in practical engineering, which has a higher sensitivity of microcracks, such as, bridge and underwater structures. Some shrinkage mitigation strategies need to be taken to minimize the microcracks in UHPC matrix. In addition, compared to the sample with silica fume, the sample with nano-silica results in a higher relative proportion of high density C–S–H that is demonstrated to enhance the bonding property of UHPC matrix, which is beneficial for the improvement of bonding property of UHPC matrix in engineering applications.

Fig. 14. Compressive strength and flexural strength of UHPC-CA containing nano-silica and silica fume. (a) Compressive strength of UHPC and UHPC-CA containing nano-silica; (b) Flexural strength of UHPC and UHPC-CA containing nano-silica; (c) Compressive strength of UHPC and UHPC-CA containing silica fume; (d) Flexural strength of UHPC and UHPC-CA containing nano-silica.
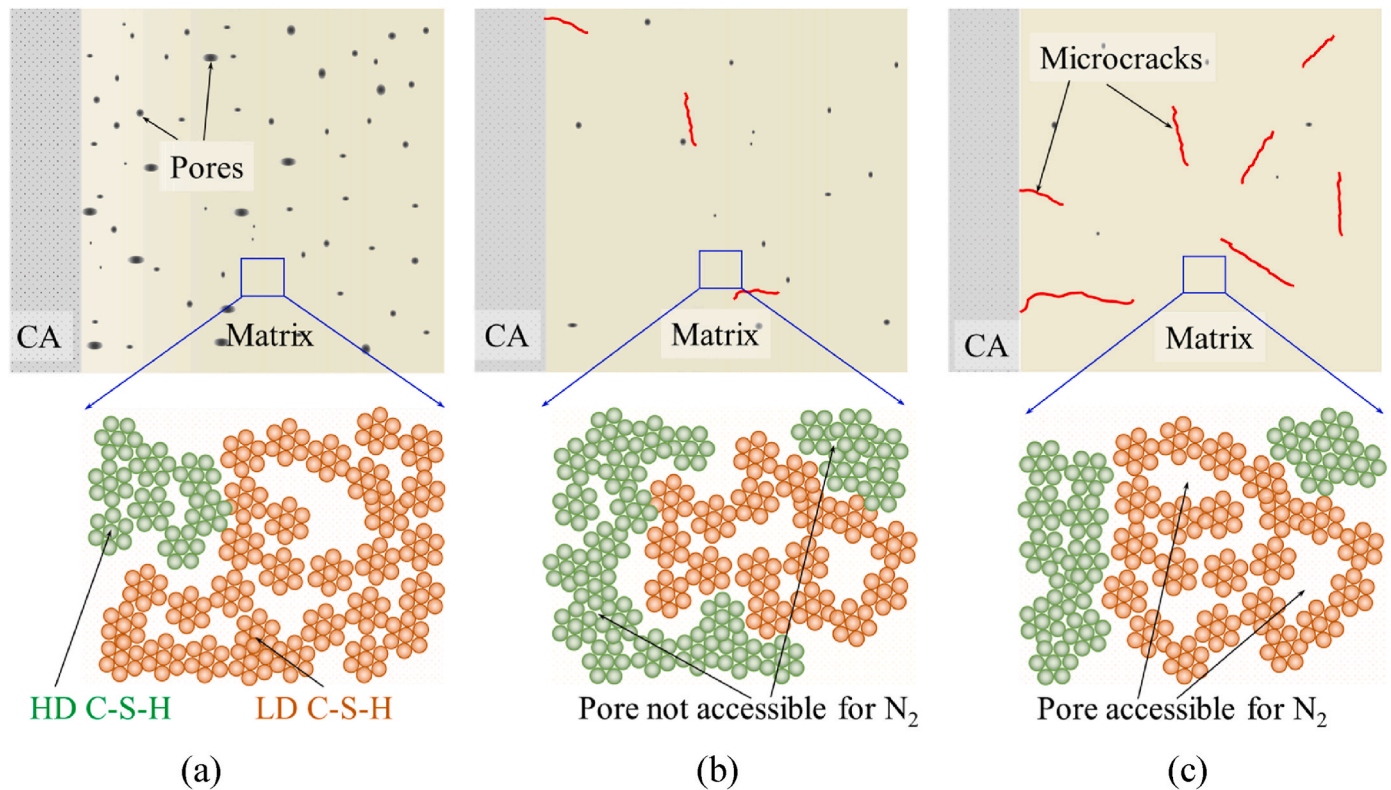

Fig. 15. Schematic of micromechanics of UHPC-CA containing amorphous silica. (a) Sample without amorphous silica; (b) Sample with 3% nano-silica; (c) Sample with 15% silica fume.

4.2. Influence of micromechanics on the mesoscale fracture of UHPC-CA

From a mesoscale perspective, the failure of UHPC-CA can be assigned to the fracture of matrix, ITZ and CA. Hence, the fracture percentage of CA governs the mechanical contribution of CA in UHPC-CA, which in turn determines if the mechanical strength of UHPC-CA is higher or lower than that of UHPC. To elucidate the influence of micromechanics on the mechanical contribution of CA, the fracture of CA in UHPC-CA is firstly analysed based on the above results.

The fracture percentage of CA in the shear cracking condition is higher than that in the tensile cracking condition, as shown in Fig. 13. Besides, it can be seen that the compactness of UHPC increases the fracture percentage of CA under pure shear cracking condition. Nevertheless, it is noteworthy that the fracture of CA under pure tensile cracking shows an obviously different pattern. For example, even though there are more microcracks appeared in the sample with 15% silica, the fracture across CA under shear fracture is the highest, which suggests that the fracture of CA under shear cracking condition is mainly affected by the compactness of UHPC-CA. In contrast, the fracture across CA decreases from 16.4% to 14.7% as silica fume content increases from 10% to 15%, which implies that the microcracks have a vital influence on the fracture of CA in the case of tensile cracking. On the other hand, the fracture across CA in the case of the sample with 3% is the highest, i.

e. 18.5%, which in turn suggests that the content of high density C–S–H is of great importance to the fracture of CA under tensile cracking condition. From the mesoscale fracture quantification, it is suggested that the shear cracking is mainly governed by the microstructure compactness, while the tensile cracking is mainly governed by the high-density C–S–H. Moreover, the fracture of CA under tensile cracking is sensitive to microcracks, whereas, that under shear cracking is insensitive to microcracks.

Based on the results of mesoscale fracture characteristics of UHPC-CA under tensile fracture and shear fracture, a schematic mechanism of cracks propagation in UHPC-CA is proposed. As shown in Fig. 16 (a) to (c), under the tensile cracking condition, the fracture across CA is affected by the content of high-density C–S–H and microcracks in UHPC matrix. Microcracks act as the propagation routine for the newly generated crack, which minimizes the facture across CA. As presented in Fig. 16 (d)–(f), in the case of shear cracking, despite the amount of microcracks, the newly generated crack across CA increases with the increased microstructure compactness of UHPC matrix. It is noted that the schematic diagram in Fig. 15 is used to present the influence of microstructure compactness and content of high-density C–S–H on the cracking path and mesoscale failure characteristics. However, the cracking pattern shown in Fig. 15 is a statistical result, which cannot be totally in accordance with the experimental images.
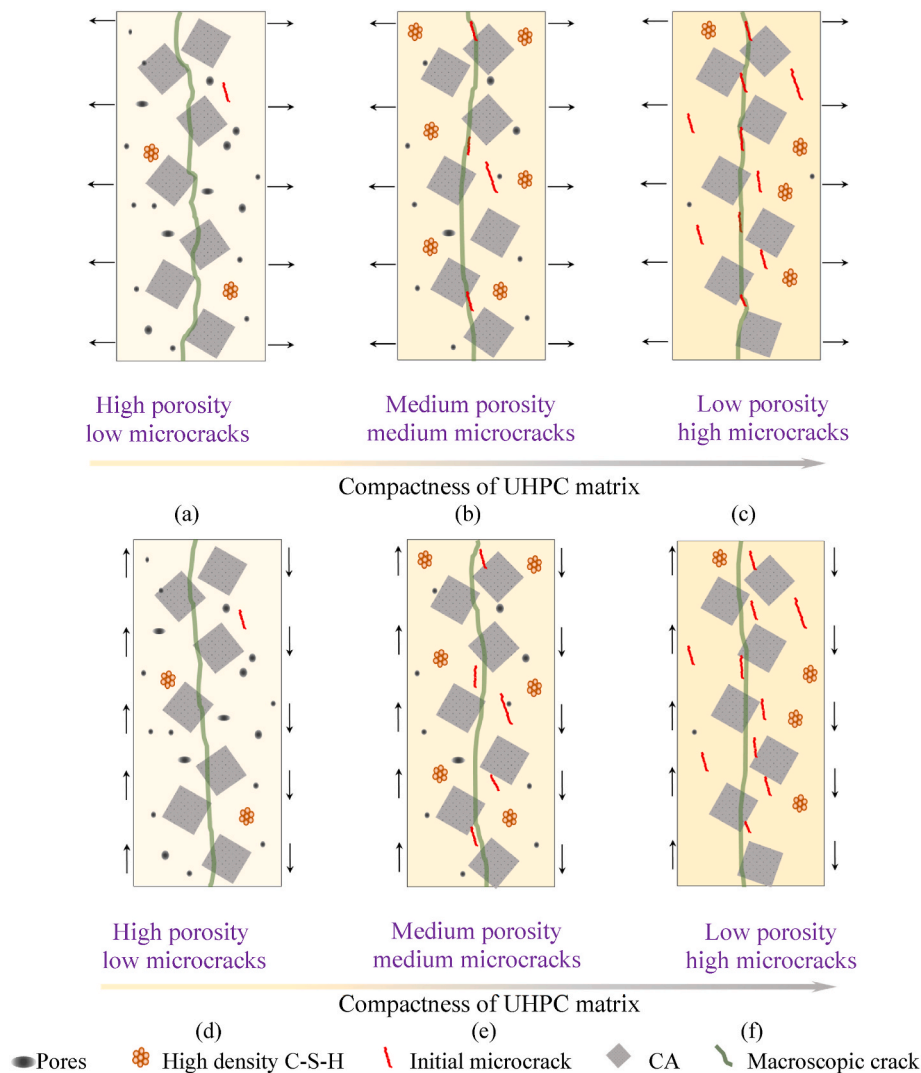

Fig. 16. Schematic diagram of crack propagation in UHPC-CA with different microscale characteristics. (a) ~ (c) UHPC-CA under tensile cracking; (d) ~ (f) UHPC-CA under shear cracking.

4.3. Influence of micromechanics on the mechanical contribution of CA in UHPC-CA

According to the previous study, the failure of concrete under compressive loading can be mainly attributed to the shearing cracking [40], whereas that under flexural loading is related to the tensile cracking [77,78]. Therefore, combining the microscale property and mesoscale fracture, it can be expected that the compressive strength of UHPC-CA is mainly governed by the microstructure compactness of the UHPC matrix, while the flexural strength of UHPC-CA is controlled by the high-density C–S–H and microcracks in UHPC matrix. Based on this, it can be deduced that, compared with the sample incorporated with silica fume, the flexural strength of the sample with nano-silica shows higher level. Meanwhile, the compressive strength improvement by the higher content of silica fume is more obvious than nano-silica. Due to the increased content of microcracks, the flexural strength of UHPC and UHPC-CA shows no obvious increase as the silica fume content increases from 10% to 15%. Moreover, as crack propagates along the existing microcracks, the fracture across matrix and ITZ increases, which in turn decreases the fracture across CA. That is, the mechanical contribution of CA decreases as long as high level of microcracks appear in ITZ and matrix.

To quantify the mechanical contribution of CA, the relative strength contribution is calculated as follows:

$$S_c = \frac{S_{UHPC-CA} - S_{UHPC}}{S_{UHPC}} \times 100\% \tag{2}$$

where $S_{UHPC-CA}$ is the strength of UHPC-CA, S_{UHPC} is the strength of UHPC, and S_c is the relative strength contribution.

The relative strength of CA in UHPC-CA is shown in Fig. 17. It is obvious that, despite the kind of amorphous silica, CA has positive contribution on the compressive strength of UHPC-CA, i.e., the strength of UHPC-CA is higher than that of UHPC. Nano-silica and silica fume have obviously different mechanical contribution on the flexural strength of UHPC-CA. Regardless of the content, silica fume has a negative influence on the flexural strength of UHPC-CA. Nevertheless, the negative effect decreases with the increase of silica fume content, which could be attributed to the increase of C–S–H content, as shown in Fig. 6, which provides a better bonding property. In addition, it is noteworthy that there is a turning point regarding the mechanical contribution of CA on the flexural strength of UHPC-CA. For example, the strength contribution of CA on the flexural strength of UHPC-CA is −0.5% in the case of 1% nano-silica, whereas it becomes 2.3% in the case of 2% nano-silica. This could be explained by the addition of nano-silica results in the increase of the total C–S–H content and the high-density C–S–H proportion, and, less microcracks compared to the sample with silica fume.

It is suggested that silica fume is more beneficial to the mechanical contribution of CA in compressive strength. However, it must be noted that too much silica fume generates more microcracks, which would compromise the mechanical contribution of CA in flexural strength. On the other hand, nano-silica can bring more mechanical contribution from CA in the case of flexural loading even though the applied content of nano-silica is significantly lower than silica fume. Thus, nano-silica can be used for the improvement of mechanical contribution of CA in the case of flexural loading condition, whereas silica fume is recommended to improve the mechanical contribution of CA in the case of compressive loading condition. However, the fracture percentage of CA in the case of compressive and flexural loading should be quantified, which is helpful to further clarify the mechanical contribution of CA. Furthermore, a model based on the mesoscale fracture mechanics is needed to link the microscopic properties and macroscopic strength. However, due to the irregular shape of CA and the heterogenous property of ITZ, the relationship between micromechanics and macroscopic strength cannot be built directly.

5. Conclusions

In this study, the influence of amorphous silica on the mechanical contribution of CA in UHPC-CA is clarified from the perspective of multiscale. The optimal addition of amorphous silica (i.e. nano-silica and silica fume) are firstly determined based on the flowability. The influence of nano-silica and silica fume on the micromechanics, mesoscale fracture and macroscopic mechanical strength of UHPC-CA are analysed. Based on the obtained results, the main conclusions can be drawn as follows:

- Considering the workability, the dosage of silica fume can be significantly higher than that of nano-silica thanks to the spherical shape and lower surface area. The maximum addition of silica fume is set as 15%, while that of nano-silica is set as 3%.
- Silica fume results in a denser microstructure along with more microcracks because of the higher content, whereas, nano-silica benefits more the generation of high density C–S–H. In the case of the sample with 15% silica fume, the porosity of matrix decreases to be 1.8%, which is lower that of the sample with 3% nano-silica. The proportion of high density C–S–H in sample with 3% nano-silica is 46%.
- The influence of amorphous silica on the fracture energy of UHPC-CA evolves with the silica type and content. In the case of nano-silica, the pure tensile fracture energy of UHPC is larger than that of UHPC-CA as the content is lower than 2%. While, in the case of silica fume, the pure tensile fracture energy of UHPC remains higher than that of UHPC-CA. However, despite the type and content of amorphous silica, the pure shear fracture energy of UHPC-CA is higher than that of UHPC.
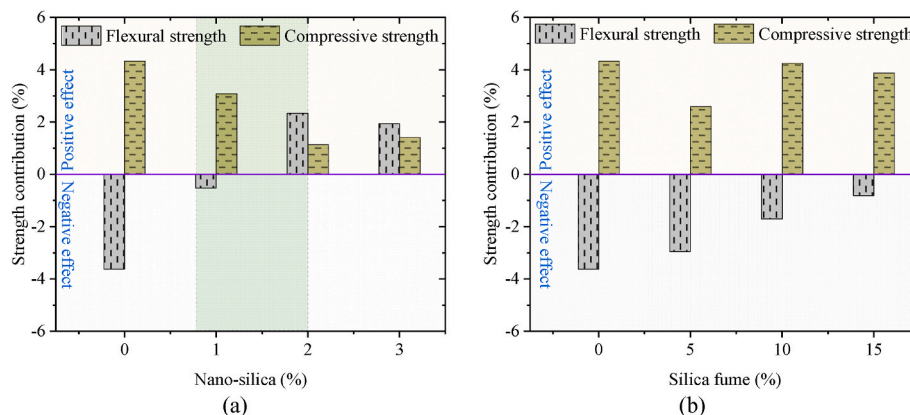

Fig. 17. Relative strength contribution of CA in UHPC-CA. (a) Sample with nano-silica; (b) Sample with silica fume.

- In the case of pure tensile cracking, the fracture across CA is controlled by the competition between the high-density C–S–H content and microcracks. In the case of pure shear cracking, the fracture across CA is more sensible to the compactness of microstructure. In addition, the fracture across CA in the pure shear fracture shows a higher level compared with the pure tensile fracture.
- Despite the kind of amorphous silica, CA has positive contribution on the compressive strength of UHPC-CA owing to the higher amount of fracture across CA in the case of shear cracking. Hence, CA is more recommended in the shear loading condition.
- Even though the C–S–H content increases with the increase of silica fume content, silica fume has negative influence on the flexural strength of UHPC-CA due to the increase of microcracks. For nano-silica, because of the higher content of high density C–S–H and less microcracks, there is a turning point, i.e., 2% nano-silica content, where the mechanical contribution of CA on the flexural strength of UHPC-CA changes from negative to positive, i.e., from -0.5% to 2.3%. Nano-silica is more suitable for the improvement of flexural strength of UHPC-CA on the premise of workability.

Declaration of competing interest

The authors declare that they have no known competing financial interests or personal relationships that could have appeared to influence the work reported in this paper.

Data availability

Data will be made available on request.

Acknowledgements

References

[1] Q. Yu, W. Zhuang, C. Shi, Research progress on the dynamic compressive properties of ultra-high performance concrete under high strain rates, Cem. Concr. Compos. 124 (2021), 104258.

[2] H. Huang, L. Teng, K.H. Khayat, X. Gao, F. Wang, Z. Liu, For the improvement of mechanical and microstructural properties of UHPC with fiber alignment using carbon nanotube and graphite nanoplatelet, Cem. Concr. Compos. 129 (2022), 104462.

[3] Y. Liu, Y. Wei, Effect of calcined bauxite powder or aggregate on the shrinkage properties of UHPC, Cem. Concr. Compos. 118 (2021), 103967.

[4] P. Shen, H. Zheng, D. Xuan, J.-X. Lu, C.S. Poon, Feasible use of municipal solid waste incineration bottom ash in ultra-high performance concrete, Cem. Concr. Compos. 114 (2020), 103814.

[5] A. Dixit, A. Verma, S. Dai Pang, Dual waste utilization in ultra-high performance concrete using biochar and marine clay, Cem. Concr. Compos. 120 (2021), 104049.

[6] J. Jiang, T. Feng, H. Chu, Y. Wu, F. Wang, W. Zhou, Z. Wang, Quasi-static and dynamic mechanical properties of eco-friendly ultra-high-performance concrete containing aeolian sand, Cem. Concr. Compos. 97 (2019) 369–378.

[7] D.-Y. Yoo, Y. Lee, I. You, N. Banthia, G. Zi, Utilization of liquid crystal display (LCD) glass waste in concrete: a review, Cem. Concr. Compos. (2022), 104542.

[8] L. Li, L. Xu, L. Huang, F. Xu, Y. Huang, K. Cui, Y. Zeng, Y. Chi, Compressive fatigue behaviors of ultra-high performance concrete containing coarse aggregate, Cem. Concr. Compos. 128 (2022), 104425.

[9] P.P. Li, Q.L. Yu, H.J.H. Brouwers, Effect of coarse basalt aggregates on the properties of Ultra-high Performance Concrete (UHPC), Construct. Build. Mater. 170 (2018) 649–659.

[10] J. Liu, F. Han, G. Cui, Q. Zhang, J. Lv, L. Zhang, Z. Yang, Combined effect of coarse aggregate and fiber on tensile behavior of ultra-high performance concrete, Construct. Build. Mater. 121 (2016) 310–318.

[11] P. Li, H.J.H. Brouwers, Q. Yu, Influence of key design parameters of ultra-high performance fibre reinforced concrete on in-service bullet resistance, Int. J. Impact Eng. 136 (2020), 103434.

[12] P. Li, Q. Yu, Responses and post-impact properties of ultra-high performance fibre reinforced concrete under pendulum impact, Compos. Struct. 208 (2019) 806–815.

[13] L. Yang, C. Shi, Z. Wu, Mitigation techniques for autogenous shrinkage of ultra-high-performance concrete–A review, Compos. B Eng. 178 (2019), 107456.

[14] S. Li, O.M. Jensen, Q. Yu, Mechanism of rate dependent behaviour of ultra-high performance fibre reinforced concrete containing coarse aggregates under flexural loading, Construct. Build. Mater. 301 (2021), 124055.

[15] Z. Yu, L. Wu, Z. Yuan, C. Zhang, T. Bangi, Mechanical properties, durability and application of ultra-high-performance concrete containing coarse aggregate (UHPC-CA): a review, Construct. Build. Mater. 334 (2022), 127360.

[16] J. Li, Z. Wu, C. Shi, Q. Yuan, Z. Zhang, Durability of ultra-high performance concrete – a review, Construct. Build. Mater. 255 (2020), 119296.

[17] J.P. Ollivier, J.C. Maso, B. Bourdette, Interfacial transition zone in concrete, Adv. Cement Base Mater. 2 (1995) 30–38.

[18] K.L. Scrivener, A.K. Crumbie, P. Laugesen, The interfacial transition zone (ITZ) between cement paste and aggregate in concrete, Interface Sci. 12 (2004) 411–421.

[19] S. Li, O.M. Jensen, Z. Wang, Q. Yu, Influence of micromechanical property on the rate-dependent flexural strength of ultra-high performance concrete containing coarse aggregates (UHPC-CA), Compos. B Eng. 227 (2021), 109394.

[20] C. Liu, M. Zhang, Multiscale modelling of ionic diffusivity in unsaturated concrete accounting for its hierarchical microstructure, Cement Concr. Res. 156 (2022), 106766.

[21] M. Ramaniraka, S. Rakotonarivo, C. Payan, V. Garnier, Effect of Interfacial Transition Zone on diffuse ultrasound in thermally damaged concrete, Cement Concr. Res. 152 (2022), 106680.

[22] N.K. Lee, K.T. Koh, M.O. Kim, G.S. Ryu, Uncovering the role of micro silica in hydration of ultra-high performance concrete (UHPC), Cement Concr. Res. 104 (2018) 68–79.

[23] B. Toa, C. Uh, A. Fh, D. Hk, E. Gsa, Influence of amorphous silica on the hydration in ultra-high performance concrete, Cement Concr. Res. 58 (2014) 121–130.

[24] Z. Wu, K.H. Khayat, C. Shi, B.F. Tutikian, Q. Chen, Mechanisms underlying the strength enhancement of UHPC modified with nano-SiO2 and nano-CaCO3, Cem. Concr. Compos. 119 (2021), 103992.

[25] Y. Qing, Z. Zenan, K. Deyu, C. Rongshen, Influence of nano-SiO2 addition on properties of hardened cement paste as compared with silica fume, Construct. Build. Mater. 21 (2007) 539–545.

[26] A. Korpa, T. Kowald, R. Trettin, Phase development in normal and ultra high performance cementitious systems by quantitative X-ray analysis and thermoanalytical methods, Cement Concr. Res. 39 (2009) 69–76.

[27] Y. Zhou, J. Huang, X. Yang, Y. Dong, T. Feng, J. Liu, Enhancing the PVA fiber-matrix interface properties in ultra high performance concrete: an experimental and molecular dynamics study, Construct. Build. Mater. 285 (2021), 122862.

[28] T. Oertel, F. Hutter, U. Helbig, G. Sextl, Amorphous silica in ultra-high performance concrete: first hour of hydration, Cement Concr. Res. 58 (2014) 131–142.

[29] W.A. Gutteridge, J.A. Dalziel, Filler cement: the effect of the secondary component on the hydration of Portland cementPart 2: fine hydraulic binders, Cement Concr. Res. 20 (1990) 778–782.

[30] D.-Y. Yoo, T. Oh, N. Banthia, Nanomaterials in ultra-high-performance concrete (UHPC) – a review, Cem. Concr. Compos. 134 (2022), 104730, https://doi.org/10.1016/j.cemconcomp.2022.104730.

[31] E. Ghafari, H. Costa, E. Júlio, Critical review on eco-efficient ultra high performance concrete enhanced with nano-materials, Construct. Build. Mater. 101 (2015) 201–208, https://doi.org/10.1016/j.conbuildmat.2015.10.066.

[32] Y.X. Chen, S. Li, B. Mezari, E.J.M. Hensen, R. Yu, K. Schollbach, H.J.H. Brouwers, Q. Yu, Effect of highly dispersed colloidal olivine nano-silica on early age properties of ultra-high performance concrete, Cem. Concr. Compos. 131 (2022), 104564.

[33] P. Mondal, S.P. Shah, L.D. Marks, J.J. Gaitero, Comparative study of the effects of microsilica and nanosilica in concrete, Transport. Res. Rec. 2141 (2010) 6–9.

[34] O.M. Jensen, P.F. Hansen, Autogeneous relative humidity change in SF-modified cement paste, Adv. Cement Res. 7 (1995).

[35] M. Jensen, P.F. Hansen, Autog enous deformation and change of the relative humidity in silica fume-modified cement paste, Mater. J. 93 (1996) 539–543.

[36] G.-Z. Zhang, H.-K. Cho, X.-Y. Wang, Effect of nano-silica on the autogenous shrinkage, strength, and hydration heat of ultra-high strength concrete, Appl. Sci. 10 (2020) 5202.

[37] T. Xie, C. Fang, M.S.M. Ali, P. Visintin, Characterizations of autogenous and drying shrinkage of ultra-high performance concrete (UHPC): an experimental study, Cem. Concr. Compos. 91 (2018) 156–173.

[38] Z. Wu, C. Shi, K.H. Khayat, Influence of silica fume content on microstructure development and bond to steel fiber in ultra-high strength cement-based materials (UHSC), Cem. Concr. Compos. 71 (2016) 97–109.

[39] R. Yu, P. Spiesz, H.J.H. Brouwers, Effect of nano-silica on the hydration and microstructure development of Ultra-High Performance Concrete (UHPC) with a low binder amount, Construct. Build. Mater. 65 (2014) 140–150.

[40] M. Liu, F. Wang, Numerical simulation of influence of coarse aggregate crushing on mechanical properties of concrete under uniaxial compression, Construct. Build. Mater. 342 (2022), 128081.

[41] S. Bhanja, B. Sengupta, Influence of silica fume on the tensile strength of concrete, Cement Concr. Res. 35 (2005) 743–747.

[42] P. Shen, L. Lu, Y. He, F. Wang, S. Hu, The effect of curing regimes on the mechanical properties, nano-mechanical properties and microstructure of ultra-high performance concrete, Cement Concr. Res. 118 (2019) 1–13.

[43] P.D. Tennis, H.M. Jennings, A model for two types of calcium silicate hydrate in the microstructure of Portland cement pastes, Cement Concr. Res. 30 (2000) 855–863.

[44] M.J. Mac, M.H.N. Yio, H.S. Wong, N.R. Buenfeld, Analysis of autogenous shrinkage-induced microcracks in concrete from 3D images, Cement Concr. Res. 144 (2021), 106416.

[45] F. Efnarc, Specification and guidelines for self-compacting concrete, Eur. Fed. Spec. Constr. Chem. Concr. Syst. 1 (2002) 1–32.

[46] B.S. EN, 12390-2, Testing Hardened Concrete-Part 2: Making and Curing Specimens for Strength Tests, Br. Stand. Inst., 2009.

[47] D. Davydov, M. Jirasek, L. Kopecký, Critical aspects of nano-indentation technique in application to hardened cement paste, Cement Concr. Res. 41 (2011) 20–29.

[48] J.Z. Bao, X.X. Dong, S.P. Chi, K.L. Scrivener, Characterization of interfacial transition zone in concrete prepared with carbonated modeled recycled concrete aggregates, Cement Concr. Res. 136 (2020), 106175.

[49] G. Fang, M. Zhang, The evolution of interfacial transition zone in alkali-activated fly ash-slag concrete, Cement Concr. Res. 129 (2020), 105963.

[50] Y. Luo, S.H. Li, K.M. Klima, H.J.H. Brouwers, Q. Yu, Degradation mechanism of hybrid fly ash/slag based geopolymers exposed to elevated temperatures, Cement Concr. Res. 151 (2022), 106649.

[51] M.R. Ayatollahi, M.R.M. Aliha, Fracture toughness study for a brittle rock subjected to mixed mode I/II loading, Int. J. Rock Mech. Min. Sci. 44 (2007) 617–624.

[52] W. Oliver, G. Pharr, An improved technique for determining hardness and elastic madulus using load and displacement, Polym. Sci. u.s.s.R. 7 (1992) 1564–1583.

[53] A. Zhh, A. Sgd, C.B. Deng, Microstructure of ultra high performance concrete containing lithium slag - ScienceDirect, J. Hazard Mater. 353 (2018) 35–43.

[54] M. Vandamme, F.-J. Ulm, P. Fonollosa, Nanogranular packing of C–S–H at substochiometric conditions, Cement Concr. Res. 40 (2010) 14–26.

[55] Y. Lin, J. Yan, Z. Wang, F. Fan, C. Zou, Effect of silica fumes on fluidity of UHPC: experiments, influence mechanism and evaluation methods, Construct. Build. Mater. 210 (2019) 451–460.

[56] C. Shi, D. Wang, L. Wu, Z. Wu, The hydration and microstructure of ultra high-strength concrete with cement–silica fume–slag binder, Cem. Concr. Compos. 61 (2015) 44–52.

[57] W. Huang, H. Kazemi-Kamyab, W. Sun, K. Scrivener, Effect of cement substitution by limestone on the hydration and microstructural development of ultra-high performance concrete (UHPC), Cem. Concr. Compos. 77 (2016) 86–101.

[58] Deyu Kong, Senle Huang, David Corr, Shah Yang, P. Surendra, Whether do nano-particles act as nucleation sites for C-S-H gel growth during cement hydration? Cem. Concr. Compos. 87 (2018) 98–109.

[59] T. Oertel, U. Helbig, F. Hutter, H. Kletti, G. Sextl, Influence of amorphous silica on the hydration in ultra-high performance concrete, Cement Concr. Res. 58 (2014) 121–130.

[60] U. Sharma, L.P. Singh, B. Zhan, C.S. Poon, Effect of particle size of nanosilica on microstructure of C-S-H and its impact on mechanical strength, Cem. Concr. Compos. 97 (2019) 312–321.

[61] M.H. Zhang, C.T. Tam, M.P. Leow, Effect of water-to-cementitious materials ratio and silica fume on the autogenous shrinkage of concrete, Cement Concr. Res. 33 (2003) 1687–1694.

[62] S.I. Igarashi, A. Bentur, K. Kovler, Autogenous shrinkage and induced restraining stresses in high-strength concretes, Cement Concr. Res. 30 (2000) 1701–1707.

[63] Ghafari, Ehsan, Ghahari, S. Ali, Costa, Hugo, Julio, Eduardo, Portugal, Antonio, Effect of Supplementary Cementitious Materials on Autogenous Shrinkage of Ultra-high Performance Concrete, Constr. Build. Mater. (n.d.).

[64] S. Diamond, Considerations in Image Analysis as Applied to Investigations of the ITZ in Concrete, vol. 23, 2001, pp. 171–178.

[65] C.S. Poon, Z.H. Shui, L. Lam, Effect of microstructure of ITZ on compressive strength of concrete prepared with recycled aggregates, Construct. Build. Mater. 18 (2004) 461–468.

[66] C. Shi, Z. Wu, J. Xiao, D. Wang, Z. Huang, Z. Fang, A review on ultra high performance concrete: Part I. Raw materials and mixture design, Construct. Build. Mater. 101 (2015) 741–751.

[67] O.M. Jensen, P.F. Hansen, Autogenous deformation and change of the relative humidity in silica fume-modified cement paste, ACI Mater. J. 7 (1995) 539–543.

[68] Y.W. Chan, S.H. Chu, Effect of silica fume on steel fiber bond characteristics in reactive powder concrete, Cement Concr. Res. 34 (2004) 1167–1172.

[69] P. Mondal, S.P. Shah, L. Marks, A reliable technique to determine the local mechanical properties at the nanoscale for cementitious materials, Cement Concr. Res. 37 (2007) 1440–1444.

[70] J.J. Chen, L. Sorelli, M. Vandamme, F.J. Ulm, G. Chanvillard, A coupled nanoindentation/SEM-EDS study on low water/cement ratio Portland cement paste: evidence for C-S-H/Ca(OH)2 nanocomposites, J. Am. Ceram. Soc. 93 (2010) 1484–1493.

[71] L. Xu, F. Deng, Y. Chi, Nano-mechanical behavior of the interfacial transition zone between steel-polypropylene fiber and cement paste, Construct. Build. Mater. 145 (2017) 619–638.

[72] S.M. Elzafraney, Damage effects on concrete performance and microstructure, Cem. Concr. Compos. 26 (2004) 853–859.

[73] B. Erzar, P. Forquin, Experiments and Mesoscopic Modelling of Dynamic Testing of Concrete, (n.d.).

[74] J. Weerheijm, I. Vegt, K. V Breugel, Failure Mechanisms of Concrete under Impact Loading, Fail. Mech. Concr. Under Impact Load. (n.d.).

[75] F. Wu, L. Xu, Y. Chi, Y. Zeng, F. Deng, Q. Chen, Compressive and flexural properties of ultra-high performance fiber-reinforced cementitious composite: the effect of coarse aggregate, Compos. Struct. (2020), 111810.

[76] P. Mondal, S.P. Shah, L.D. Marks, J.J. Gaitero, Comparative study of the effects of microsilica and nanosilica in concrete, Transport. Res. Rec. 13 (2015) 6–9.

[77] G. Meng, B. Wu, S. Xu, J. Huang, Modelling and experimental validation of flexural tensile properties of steel fiber reinforced concrete, Construct. Build. Mater. 273 (2021), 121974.

[78] M. Shafieifar, M. Farzad, A. Azizinamini, A comparison of existing analytical methods to predict the flexural capacity of Ultra High Performance Concrete (UHPC) beams, Construct. Build. Mater. 172 (2018) 10–18.